

Ultrarobust, tough and highly stretchable self-healing materials based on cartilage-inspired noncovalent assembly nanostructure

Yuyan Wang

Sichuan University

Xin Huang

Sichuan University

Xinxing Zhang (✉ xxzwwh@scu.edu.cn)

Sichuan University

Article

Keywords: self-healing materials, cartilage-inspired noncovalent assembly nanostructure, nanocomposite

Posted Date: October 13th, 2020

DOI: <https://doi.org/10.21203/rs.3.rs-89039/v1>

License:   This work is licensed under a Creative Commons Attribution 4.0 International License.

[Read Full License](#)

Version of Record: A version of this preprint was published at Nature Communications on February 26th, 2021. See the published version at <https://doi.org/10.1038/s41467-021-21577-7>.

Ultrarobust, tough and highly stretchable self-healing materials based on cartilage-inspired noncovalent assembly nanostructure

Yuyan Wang¹, Xin Huang¹ & Xinxing Zhang^{1*}

¹ State Key Laboratory of Polymer Materials Engineering, Polymer Research Institute, Sichuan University, Chengdu 610065, China

Correspondence and requests for materials should be addressed to X.Z. (email: xxzwwh@scu.edu.cn)

Abstract: Self-healing materials integrated with robust mechanical strength and high healing efficiency simultaneously would be of great use in many fields but have been proven to be extremely challenging. Here, inspired by animal cartilage, we present a ultrarobust self-healing material by incorporating high density noncovalent bonds at interface between the assembled interwoven network of two-dimensional nanosheets and polymer matrix to collectively produce a strong interfacial interaction. The resulted nanocomposite material shows robust tensile strength (52.3 MPa), high toughness (282.7 MJ m⁻³, which is 1.6 times higher than spider silk and 9.4 times higher than metallic aluminum), high stretchability (1020.8%) and excellent healing efficiency (80-100%), which overturns previous understanding of the traditional noncovalent bonding self-healing materials that high mechanical robustness and healing ability tend to be mutually exclusive. Moreover, the interfacial supramolecular crosslinking structure enables the functional-healing ability of the resultant flexible devices. This work opens an avenue toward the development of ultrarobust self-healing materials for various flexible functional devices.

Highly strong, self-healable, and stretchable materials have been increasingly desirable recently as indispensable functional devices for their potential applications in electronic skin¹⁻⁶, wearable electronic devices⁷⁻¹², and artificial muscles, etc.¹³⁻²⁰. The healing of damage in

polymers can be realized through the reversibility of dynamic bonds that cross-link polymer chains, which is able to extend the service life and improve reliability and durability of functional devices. But self-healing materials prepared by single noncovalent bond are limited to their low strength, especially self-healing hydrogels and elastomers are usually below 3.0 MPa^{21–27}. Hence, there exists a long-standing challenge to acquire flexible composites integrated with high stretchability, outstanding mechanical strength and self-healing ability at the same time, because these factors tend to be mutually exclusive in conventional thinking.

To date, most of self-healing materials can not break the tensile strength of 10.0 MPa^{28–32} due to the low strength nature of noncovalent bonds and the weak interfacial interaction between fillers and polymer matrix. Introducing multiple dynamic bonds into polymeric materials have been proposed to deal with the trade-offs in fabricating high-performance self-healing materials. Aida et. al. reported a low-molecular weight polymer by multiple noncovalent cross-linking with tensile strength up to 26.5 MPa³³. Xi Zhang and co-workers designed and fabricated both reversible noncovalent bonds and permanent covalent crosslinks to improve mechanical strength to 34.0 MPa³⁴. In most cases for self-healing materials, their mechanical strength are still relatively low and not capable of meeting the requirement of structural materials.

In nature, the cartilage tissue of animals meets the requirements of the above proposed structural materials, which has high mechanical strength and a certain self-healing ability after being damaged. The side chains of proteoglycan molecules in cartilage matrix are connected with collagen fibers through hydrogen bonds to form a network structure, and a large number of collagen fibers are interwoven into a network which can bear the force. Previously, a number of studies have combined woven fiber networks or hard plastic skeletons with soft matrix to

achieve ultrahigh mechanical properties of composites^{35–38}. This undoubtedly proves the effectiveness of the cartilage-like structure strategy of assembling a rigid "skeleton" into a flexible matrix by strong adhesion. However, since it is a macroscopic assembly of rigid networks and soft matrix, it is difficult for above composites to achieve highly stretchability.

Here, we propose a cartilage-inspired micro-/nano- scale assembly route to fabricate ultrarobust self-healing materials based on a noncovalent bonding driven self-assembled two-dimensional (2D)-nanosheets interwoven network. The interwoven network connected with dense hydrogen bonds aggregated at the interface endows the resulted composites with remarkably improved mechanical properties and self-healing efficiency, as well as excellent functional-healing ability of the developed flexible devices. Our results suggest an exciting material platform of high-performance self-healing materials, which could be applied to a wide range of flexible functional devices.

Results

Material design and characterization. The structure of organs and tissues of living systems in nature is a valuable resource for the construction of novel materials and gives precious inspiration to the structural design of materials. For example, human cartilage tissue is composed of collagen cells and intercellular substance (Fig. 1a). A large number of collagen nanofibrils interlinking with cartilage matrix by hydrogen bonding, which interwoven into a network to bear the force (Fig. 1b). Therefore, such hierarchical structure with strong supramolecular interactions makes cartilage mechanical strong and tough. Recently, ultra-thin 2D tungsten disulfide (WS₂) nanomaterials have attracted widespread attention for their excellent physical and chemical properties. However, its high rigidity and poor interfacial interaction with soft matrix make it difficult to adequately play a role in flexible devices. At

present, there is still lacking suitable route to assemble such rigid active 2D materials into appropriate polymer substrates to form self-healing materials. Combining high-performance materials with rational bionic structure design is a versatile strategy to develop smart materials and flexible devices. Here, we embed a noncovalent bonding driven self-assembled WS₂ network in waterborne polyurethane (PU) matrix to mimic the interwoven network structure of collagen fibrils in cartilage (Fig. 1c).

Based on a tannin acid (TA)-assisted exfoliation strategy³⁹, we facilely exfoliate WS₂ into monolayer or few-layer nanosheets through hydrophobic interaction between the 2D monolayer and hydrophobic aromatic structures in polyphenols. Then we further utilize the polyhydroxy structure of TA adsorbed on the nanosheets to construct and regulate the aggregation density of hydrogen bonds at the interface between 2D WS₂ nanosheets and PU matrix. This assembly process can retain the excellent physical and chemical properties of WS₂, and also has strong adhesion and lubricating characteristics to combine with PU matrix. Thus, the interwoven network of 2D WS₂ and the high-density hydrogen bonds at the interface synergistically endow the materials with high strength, ultra-tough, and excellent self-healing abilities.

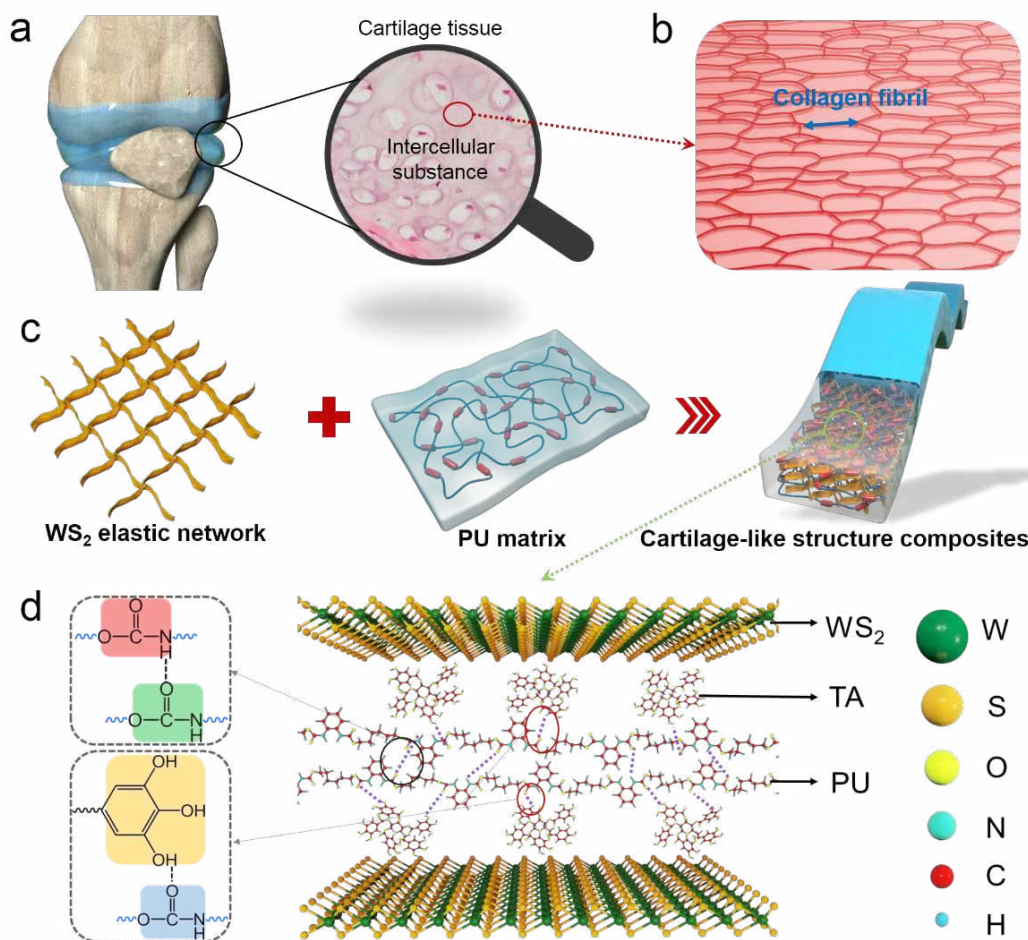


Fig. 1 The nanostructure design of the cartilage-like PU composite. **a** Schematic illustration of a cartilage structure. **b** Schematic illustration of intercellular substance of cartilage tissue. **c** Schematic illustration of the nanostructure of composite consisting of hydrogen bonded interwoven network of 2D WS₂ and PU matrix. **d** Schematics of the dynamic noncovalent bonding interaction between PU and interwoven network of 2D WS₂.

The as-prepared WS₂ nanosheets were evaluated by transmission electron microscopy (TEM), as shown in Fig. 2a. It presents a high-magnification TEM image, which unambiguously reveals the presence of a well exfoliated WS₂ nanosheet. Particle size analysis of TA-modified WS₂ dispersion solution (Supplementary Fig. 1) shows that WS₂ nanosheets have an average size of 100 nm. The X-Ray Diffraction (XRD) pattern of the WS₂ nanosheets reveals highly crystalline WS₂ phase with (002, 004, 100, 101, 103, 006, 105, 110, and 008) peaks identical to those of

bulk WS₂ (JCPDS Card No. 08-0237) as shown in Fig. 2b^{40,41}. The interlayer distance calculated according to Bragg's equation is 0.6 nm. From the Raman spectrum of WS₂ bulk (Fig. 2c), two characteristic bands located at 349.8 cm⁻¹ (E_{2g}¹) and 417.3 cm⁻¹ (A_{1g}) can be clearly distinguished. It is well known that the resonant Raman scattering of 2D materials is layer dependent^{42,43}. After exfoliation, these frequencies generally undergo small variations due to decreased interlayer interactions, i.e., the E_{2g}¹ band up-shifts while the A_{1g} band downshifts, further indicating the presence of few-layer WS₂ nanosheets^{44,45}.

In addition, the unique dendritic polyhydroxy character of TA allows the individual WS₂ nanosheets to be scaffolded to prevent aggregation. The absorbance change results in the UV-vis absorption spectra (Supplementary Fig. 2), indicating the as-exfoliated nanosheets can form highly stabilized dispersions without the appearance of aggregation phenomenon even when incubated for 30 days. The Zeta potential of the TA-stabilized WS₂ nanosheets is -34.2 mV (Supplementary Fig. 3), which further indicates the stability of the nanosheets dispersion. After one week of dialysis, the obtained WS₂ nanosheets still attached ~14.7% TA (as shown in Fig. 2d and Supplementary Fig. 4)⁴⁶, as quantitatively measured by thermogravimetric analysis (TGA). This is a result of the fascinating adhesion forces based on the catechol-inspired chemistry via multiple noncovalent interactions, and the origin of their interaction is mainly

attributed to the hydrophobic interaction between the WS₂ monolayer and hydrophobic aromatic structures in polyphenols⁴⁷.

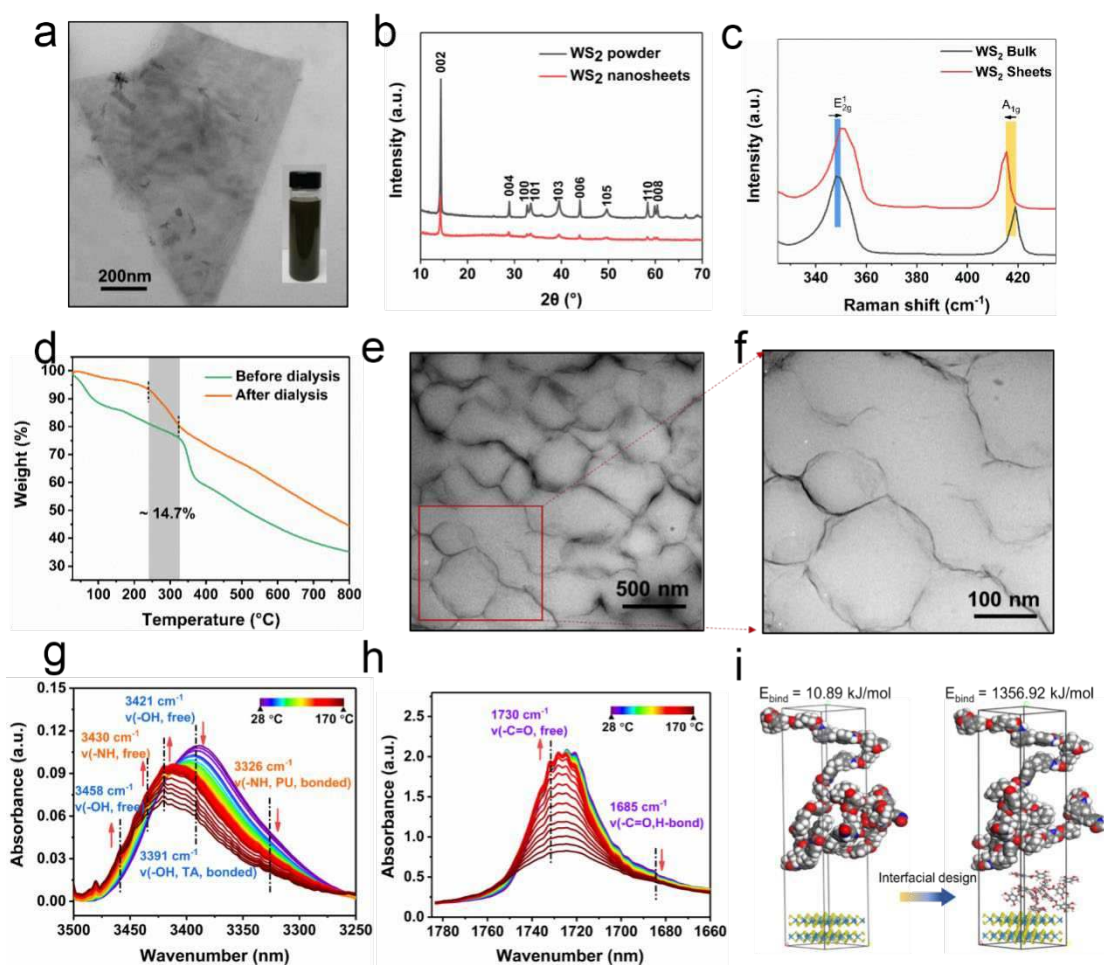


Fig. 2 Structural and compositional characterizations. **a** High-resolution TEM images of the exfoliated WS₂ nanosheet. **b** XRD patterns of WS₂ powder and WS₂ nanosheets. **c** Raman spectra of WS₂ bulk and nanosheets. **d** TGA curve of TA-WS₂ nanosheets before and after dialysis. **e, f** TEM images of TA-WS₂/PU composites with 3D conductive network. **g, h** Temperature-dependent FTIR spectra of WS₂/PU nanocomposites upon heating from 25 to 170 °C, (**g**) 3250-3500 cm⁻¹ and (**h**) 1660-1780 cm⁻¹. **i** Optimized structures and binding energies of the before and after interfacial design.

Based on the modification and stabilization of WS₂ nanosheet by TA, we assembled a cartilage-like structured nanocomposite. The cross-section morphologies of WS₂/PU nanocomposites (Fig. 2e, f) show that there is an ordered interwoven network of WS₂ nanosheets in PU matrix, like collagen fibrils in cartilage matrix. The formation of hydrogen bonding between WS₂ and PU was investigated by temperature-dependent FTIR spectra, which has been proved a powerful tool to investigate the molecular interaction in polymers⁴⁸. The temperature-dependent FTIR spectra of TA-modified WS₂/PU upon heating from room temperature to 170 °C are shown in Fig. 2g, h. For PU, the bands at 3391 cm⁻¹ (hydrogen bonded –OH groups in TA, Supplementary Fig. 4) gradually shift to 3321 cm⁻¹. Besides, the intensity of 3326 cm⁻¹ related to hydrogen bonded –NH groups in PU⁴⁹ gradually decreases, while that of the bands at 3458, and 3430 cm⁻¹ gradually increases. These spectral features indicate that the hydrogen bonding between PU and TA-modified WS₂ gradually broken with the increasing temperature. As for the –C=O groups of WS₂/PU (Fig. 2f) composites, it is noted that the bands intensity of the hydrogen bonded –C=O group keep decreases in the whole heating process, but the peak intensity of free –C=O group around 1731 cm⁻¹ is increased^{50,51}. These results indicate the breakage of various hydrogen bonds of related groups which generates “free” –C=O groups.

Binding energy simulation between PU molecular chain and the monolayer WS₂ nanosheet (there is TA modifying or not) was employed to further understand the interaction mechanism of noncovalent bonds (Fig. 2g and h). The binding energy can be calculated according to the following equation^{52,53}:

$$E_{bind} = E_{PU} + E_{filler} - E_{total}$$

in which E_{bind} is the binding energy between PU and filler; E_{PU} and E_{filler} represent the corresponding energy of PU and filler in the optimized conformation, and E_{total} is the total

150 energy of the system. In order to compute the binding energy between PU and filler, the model
151 after molecular dynamic simulation of composite using the Universal force field should be
152 constructed to calculate E_{total} . The corresponding energy PU was calculated from the structure
153 created from the optimized conformation of composite by removing the filler without further
154 minimization, and the E_{filler} was obtained by the same way after removing all the PU out from
155 the optimized conformation of composite. Similarly, we can get the binding energy of polymer
156 matrix and fillers from the optimized conformation of nanocomposites. It is worth noting that
157 the binding energy between PU and TA-WS₂ reaches up to 1356.9 kJ/mol, whereas the binding
158 energy of PU and monolayer WS₂ nanosheets is only 10.9 kJ/mol (Fig. 2i). As a result, the
159 adsorption of TA onto the WS₂ nanosheets can supply strong binding sites for WS₂ and PU

matrix, which is expected to endow the nanocomposites with fascinating self-healing property with high mechanical performance.

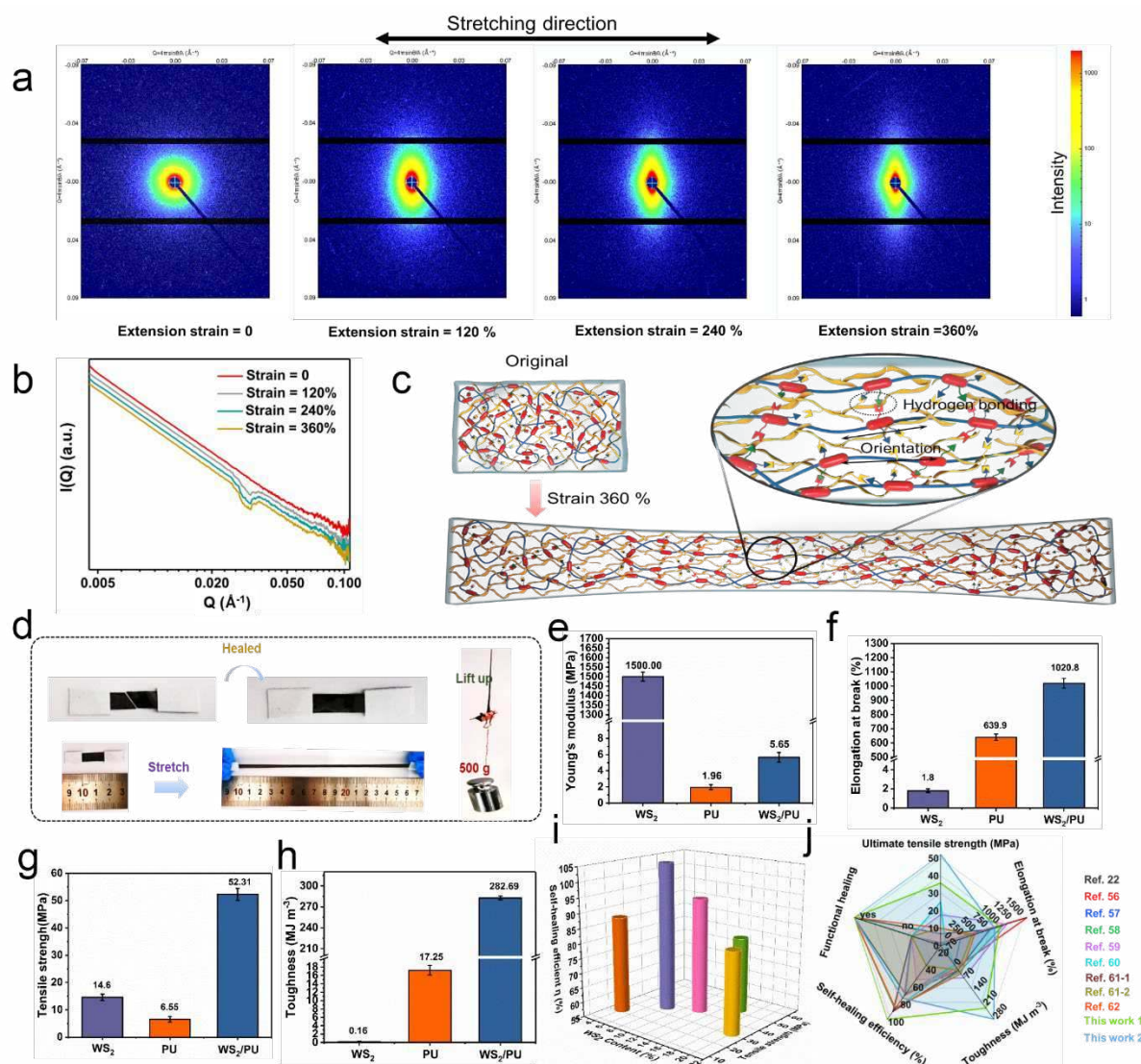


Fig. 3 Mechanical and self-healing performances. **a** 2D SAXS images of the TA-WS₂/PU with different extension strain during uniaxial stretching process. **b** 1D scattering profiles of TA-WS₂/PU integrated from 2D SAXS patterns under different strains. **c** Schematic illustrations of the nanostructure of the original sample and stretching sample. **d** Photographs demonstrating excellent mechanical property of self-healed TA-WS₂/PU composites when stretched and lift a weight. **e-h** Comparison of (e) Young's modulus, (f) elongation at break, (g) ultimate tensile strength, and (h) toughness of the pure WS₂, PU, and TA-WS₂/PU

nanocomposite. **i** Comparison of tensile strength and self-healing efficiency of our TA-WS₂/PU nanocomposite with different filler content. **j** Comparison of Young's modulus, elongation at break, ultimate tensile strength, toughness, self-healing efficiency, and functional healing ability of our nanocomposite with other self-healing materials.

Mechanical and self-healing performances. For evaluating the practicability of the nanocomposites as the functional devices, its mechanical and self-healing properties were studied in detail. Benefited from the cartilage-like nanostructure, the nanocomposites exhibit excellent mechanical and self-healing performance. To demonstrate the deformation mechanical of the composite elastomer, small angle x-ray scattering (SAXS) analysis of composite sample and control sample at different strains was conducted. The 2D scattering patterns are shown in Fig.3a. As the strain increased, the scattering signal changed from homodispersion to orientation to the equator direction, and the scattering ring become rhombic, indicating that the isotropic WS₂ network structure was oriented along the stress direction. The direction of WS₂ bearing load was consistent with the direction of external force, which could effectively bear the stress of the matrix in the tensile direction and improve the strength of the material^{54,55}. In the control sample, the oriented behavior is much weaker (Supplementary Fig. 5). Due to the lack of TA adhesion, the thickness of the interfacial layer decreased from 2.34 nm to 0.27 nm (Supplementary Fig. 6), and the WS₂ which did not form an elastic network, so that PU molecular chains could not drive the orientation of WS₂. Fig 3b and Supplementary Fig. 7 show the representative scattering profiles of composite sample and control sample under different strains, respectively. An obvious increase in the scattering peak at $q \approx 0.032 \text{ \AA}^{-1}$ with increasing strain can be observed. The peak at $q \approx 1.3 \text{ nm}^{-1}$ for composite with high strain can be ascribed to the break-reconstruction of hydrogen bonds have lower electronic density in the

stretch process, which contributes to the improvement of the mechanical strength compared with control sample.

The reinforcing mechanism for the composites is illustrated in Fig. 3c. The dendritic polyhydroxyl TA molecule loaded on WS₂ nanosheets could act as physical cross-linking points by forming hydrogen bonding interactions in PU matrix. Furthermore, during the stretching process, the interfacial hydrogen bonds between WS₂ and PU facilitated the orientation of chain segments and led to strain-induced self-reinforcement. The physical cross-linking network and the self-reinforcement during stretching enhanced the strength of elastomer. Additionally, the dynamic fracture and reconstruction of hydrogen bonds dissipated energy continually, which improved the toughness of elastomer and enabled the nanocomposite to heal when it was subject to damage. To investigate the mechanical self-healing ability, the cutting-off nanocomposite was reconnected for healing (Fig. 3d). The healed sample could stretch from 1.5 cm to 16.0 cm without break, and it could lift a weight of 500 g.

Compared with traditional noncovalent bonding connections, the special contributions of TA-modified WS₂ include the formation of a microphase separation structure in the PU matrix and provide the interfacial dynamic hydrogen bonds. This structural construction could form a strong physical cross-linking network and restrain the PU chain segments to facilitate the strain-induced microphase separation, leading to a much stronger tensile strength and toughness of nanocomposites. As a result, the mechanical properties of our micro-/nano- scale assembled cartilage-like nanocomposites are dramatically improved, with the highest tensile strength of 52.3 MPa, toughness of 282.7 MJ m⁻³, and elongation at break of 1020.8%, respectively, which are about 1.6, 8.0, 16.4 and 2.9 times those of the pristine PU (Fig. 3e-h). Compared with other PU composites filled with rigid fillers (graphene, cellulose nanocrystalline, carbon nanotube,

etc.), the as-prepared nanocomposite also shows outstanding mechanical performance (Supplementary Fig. 8), which further demonstrates the effectiveness of the controlled assembly of 2D materials and strong interfacial interaction design. The mechanical and self-healing performances of WS₂/PU composites with various filler content and hydrogen bonds density were measured by tensile tests (Fig. 3i), and the typical stress–strain curves are shown in Supplementary Fig. 9. The tensile strength and toughness of the measured WS₂/PU composites increase but then decrease with the increase in WS₂ contents of the WS₂/PU composites. The 16%-WS₂/PU composite shows the optimal mechanical performance with the self-healing efficiency of 80.6% due to the highest density of hydrogen bonds between the components. And the 8%- WS₂/PU composite exhibits the highest self-healing efficient (105.1%) without any external assistance. However, as the substitution amount of WS₂ reaches 20%, the mechanical performance of the elastomer abruptly decreases, probably due to the aggregation of WS₂ in the PU matrix, and the excess WS₂ also hindered the movement of polymer chain segments to restricted the recovery of break hydrogen bonds.

The mechanical and self-healing properties of the nanocomposites exceed those of most self-healing polymers (Fig. 3j, details in Supplementary Table 1)^{22,56–62}, which makes them attractive for applications in flexible devices. Notably, the toughness of the 16%-WS₂/PU composite (282.7 MJ m⁻³) outperforms most polymer structural materials. For instance, its toughness is 1.6 times higher than that of the ultrastrong dragline fiber of spider. Most remarkably, the toughness of the composite is much higher than that of plastic, like polyether-ether-ketone (16.3 MJ m⁻³), polyamide (38.8 MJ m⁻³), high density polyethylene (151.2 MJ m⁻³). Thanks to the reversible hydrogen bonding crosslinking networks (Fig. 4a), our self-healing material has two distinctive advantages: i) it exhibits relatively high mechanical ultimate

strength and stretchability, which make it more robust than other elastomers for further applications. ii) It can heal itself at room temperature with great self-healing efficiency and heal function. Thereby, the incorporation of nanofillers into polymer matrices *via* noncovalent bonding connection is an effective strategy to fabricate highly strong and tough nanocomposites, which provides a guidance to design self-healing structural materials.

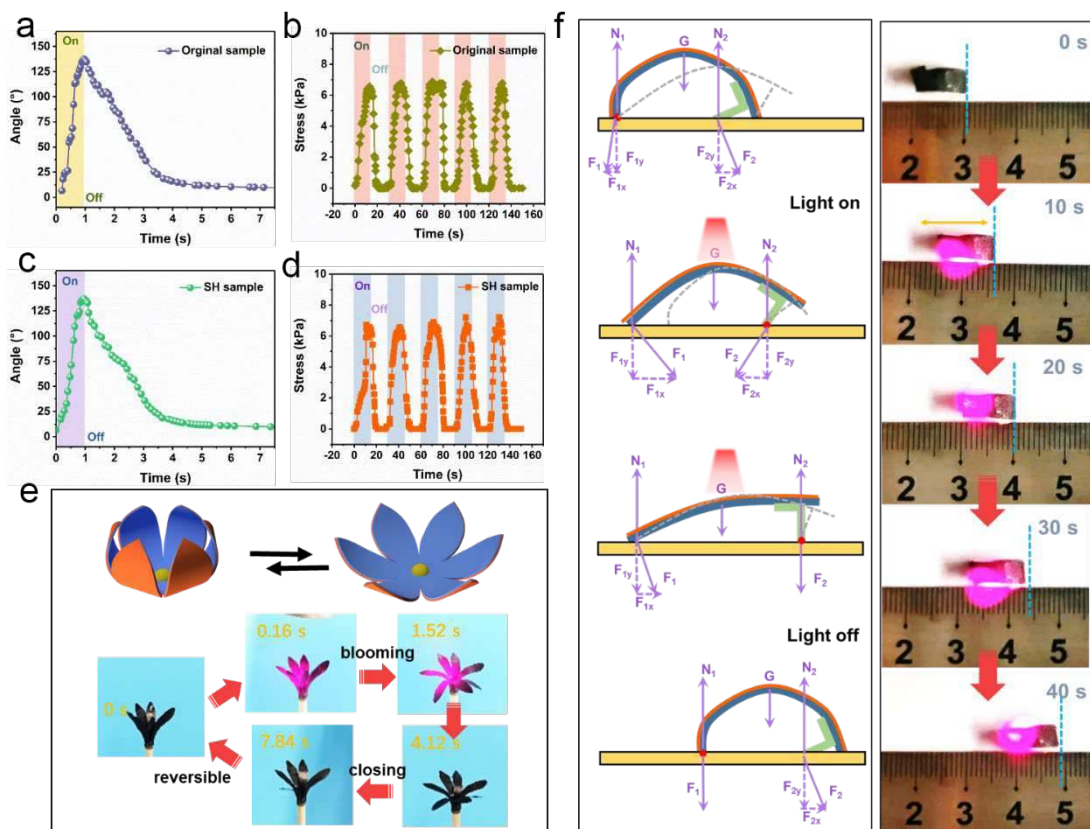


Fig. 4 NIR light actuating and self-healing performances. **a, c** Time dependence of the bending angle of (a) the original sample and (c) SH sample exposed to NIR light when the light is switched on and off. **b, d** Actuation stress as a function of time as NIR light is periodically turned on (time, 15 s) and off (time, 15 s) on (b) the original and (d) SH sample. **e** Photographs of a “flower” blooming and closing stimulated by NIR light. **f** A crawling robot is able to continually crawl forward under periodic NIR light on and off.

Robust NIR actuation and self-healing performances. Some previously reported self-healing materials have achieved excellent healing capability, but many of them can only heal

polymer matrix, functional filler network could not be repaired so that fine structure is easy to be damaged. As a demonstration, we fabricated near-infrared (NIR) actuators based on the mismatch of thermal expansion between two layers. Benefiting from the unique interconnected network design, the as-prepared material exhibits rapid photothermal conversion and heat transfer rate (Supplementary Fig. 10). The high photothermal conversion and heat transfer rate endow the nanostructured composites with excellent NIR actuating performance (Supplementary Fig. 11). As shown in Fig. 4a, it takes only 0.9 seconds to bend to maximum angle (137°) for the strip-shaped sample. The photo-induced mechanical force under NIR light irradiation was investigated as shown in Fig. 4b, under irradiation with NIR light, the actuator generates a large stress that increases with the light intensity, reaching about 6.9 kPa for the light power of 0.6 W. When turning off the NIR light, the stress is dropped with a significant amount and then goes down to zero quickly. The cycle of force up and down with NIR light on and off, respectively, which can be repeated for 5 times without damping. Besides, the actuating properties of the nanocomposite can also be restored after self-healing at room temperature.

Interestingly, the self-healed (SH) sample has the same actuating speed and amplitude as the original sample (Fig. 4c), and generates similar actuation stress compared with the original sample (Fig. 4d). The cycle of force up and down can be repeated upon NIR light on and off, which demonstrates high reliability and stability of our actuators without apparent fatigue with fast NIR responsiveness. A biomimetic flower was fabricated which can undergo repeated closing and blooming in response to NIR (808 nm, 0.6 W) on and off (Fig. 4e, Supplementary Movie 1). The temperature variation during the blooming actuation could be observed in IR images (Supplementary Fig. 12). The crawling robot exhibits step-by-step crawling behavior upon NIR light on and off (Fig. 4f, Supplementary Movie 2, details of force analysis in

Supplementary Note 1). We believe the ultrarobust flexible devices with excellent self-healing ability has great potential in broad scientific and engineering fields.

Discussion

In summary, we have developed a cartilage-inspired ultrarobust self-healing material by incorporating high density noncovalent bonds at the interface to collectively produce a strong adhesive force between assembled interwoven network of 2D nanosheets and polymer matrix. The dynamic nature of the noncovalent bonds allows them to be broken and re-formed during stretching, which leads to unfolding of the polymer chains and significantly increasing the thickness of the interfacial layer. In addition, the interwoven network of 2D nanosheets is similar to collagen nanofibrils in collagen matrix interwoven into a network to bear the force, which enables high stretchability, robustness and self-healable ability of the material. We believe that the material's micro-/nano- scale structural design and high performance make it promising for artificial muscle applications, and envisage that the design concepts presented here may represent a general approach to the preparation of highly strong functional materials.

Methods

Materials. Tungsten disulfide (WS_2), Tannic acid (1.7 kDa, AR) was obtained from Shanghai Aladdin Biological Technology Co., LTD (China). Waterborne polyurethane (PU) was purchased from Bayer Co., LTD (China). Cellulose nanofibers (CNF) 1% dispersion solution was purchased from Guilin Qihong Technology Co.,LTD (China). All the reagents were used as received without further purification. The water used in all experiments was deionized and ultrafiltered to $18.2 \text{ M}\Omega\cdot\text{cm}$ with a Ulupure ultrapure water system.

Polyphenol-Assisted Exfoliation of WS_2 . The exfoliation process was executed using an ultrasonic cell crusher with a tunable power from 0 to 1500 W. The tip of the ultrasonic cell crusher can utilize strong ultrasound to produce a cavitation effect in liquid to cause the solid particles or cellular tissue in liquid to

break up, which is a more powerful ultrasonic method than that of a conventional bath sonication treatment. In brief, 240 mg of WS₂ powder was added into a 120 mL aqueous solution containing 120 mg of tannic acid, and then the suspensions were sonicated under 300 W for 2 h. Finally, the supernatant WS₂ nanosheets were collected after centrifugation at 6000 rpm for 15 min to remove unexfoliated WS₂. Note that ultrapure water (pH \approx 6.0) was used during all the exfoliation experiments to prevent the aggregation of exfoliated nanosheets *via* oxidative cross-linking of polyphenols.

Preparation of WS₂/PU nanocomposites. Firstly, different amounts of TA-WS₂ suspensions were added into the PU latex suspension (1 g, 60 wt%) and were stirred for 30 min. Next, the TA-WS₂/PU film were fabricated via vacuum filtration of the mixed TA-WS₂/PU latex suspension on a PP filter membrane with 0.22 μ m pore size to ensure the retained of the TA-WS₂/PU film on the filtration membrane. The resultant films were left in air at room temperature for 4 h to dry and then peeled off from the polypropylene membrane. The weight ratio of and TA-WS₂ and PU was 4%, 8%, 12%, 16%, and 20%, respectively.

Preparation of actuators. The CNF 1% dispersion solution was passed through the vacuum filtrated through a cellulose nitrate film to prepare freestanding CNF film. Once CNF film appeared to be dried, 10 mL TA-WS₂/PU latex was dispensed through it to form a bilayer film. The resulted nanocomposite film was left for air-drying at room temperature until it detached by itself from the cellulose nitrate membrane.

Fabrication of bionic robots with reversible actuation. The difference of thermal expansivity between the two sides of the film makes it possible to change shapes upon NIR light on and off. The patterned actuator was fabricated with the help of origami or kirigami method. The reversible actuating performance was carried out by controlling the NIR light on and off with the help of commercial NIR laser device. As for the NIR response of the 2D film, the actuation angle of the film increases with the increase of NIR light power. Next, the actuation angle gradually decreases and the sample return to the original 2D film shape with NIR light

and turning off. The actuation movement of samples were obtained by a digital camera (D7100, Nikon), and the data of the actuation angles were captured from the camera record.

Characterization. Transmission electron microscopy (TEM) was performed on a transmission electron microscope (JEOL JEM-100CX, Japan). The X-Ray diffraction (XRD) pattern was recorded from 10° to 70° using a Philips Analytical X'Pert X-diffractometer (The Netherlands) with Cu K α radiation ($\lambda = 0.1540$ nm). Laser confocal microscopy Raman spectroscopy (HORIBA, HR Evolution, Japan) with a 532 nm laser line was performed to characterize the exfoliation of WS₂. The exfoliation concentration and yield of as-obtained WS₂ nanosheet dispersions were calculated by measuring the mass of WS₂ after freeze-drying the exfoliated dispersions (adsorbed TA on as-exfoliated nanosheet surface was subtracted from TGA analysis). Fourier transform infrared (FTIR) spectroscopy was performed from 3500 to 700 cm⁻¹ on a Nicolet 6700 spectrophotometer (USA). Mechanical properties measurements were conducted on a universal tensile testing machine (Instron-5560, USA) with an extension rate of 100 mm min⁻¹ at room temperature. Super deep scene 3D microscope was performed to detect the fractured surface morphology of self-healed sample. The infrared imaging device (Fluke Ti400, USA) was performed to detect the temperature distribution of the samples.

Bind energy simulation. A simulated annealing method was used to evaluate the interfacial design of the material system. It was performed under a cvff force field in Material Studio 2018 with the Adsorption Locator module. First, all the molecules and the WS₂ (0 0 1) layer were constructed and geometrically optimized using the Forcite module. The WS₂ layer was modeled using 12×12 supercells. The vacuum slam was set as 50 Å to avoid any nonbonding interactions between two adjacent layers. Then, in performing the Adsorption Locator simulation, the molecule was randomly distributed over the WS₂ layer. The optimal configuration was determined by carrying out a Monte Carlo simulation on the configurational space of the molecule within the surface region. The max adsorption distance was set as 15 Å.

Temperature-dependent FTIR spectroscopy. A Nicolet iS50 Fourier transform spectrometer (U.S.A.) equipped with a deuterated triglycine sulfate (DTGS) detector was used for the temperature-dependent FTIR experiments. The TA- WS₂ with PU composite films were firstly sandwiched between two CaF₂ windows, and then placed into a home-made in-situ pool (programmable heating device). The films were heated from 25 to 170 °C at 5 °C/min. Each FTIR spectrum was obtained from 20 scans with a resolution of 4 cm⁻¹, and totally 65 spectra was gathered during heating. During the experiment, the samples were protected by high-purity nitrogen gas (200 mL/min).

In-situ stretching-SAXS measurement. Scattering data were obtained from a small-angle X-ray scattering (SAXS) apparatus Xeuss 2.0. The incident x-ray beam with an energy of 15 keV was used, and it was normal to the sample film so that the SAXS was in transmission geometry. A Rayonix MX225-HE CCD x-ray detector was used, with a sample-to-detector distance of 3489.2 mm. The 2D CCD images were then reduced into scattering intensity (I) as a function of scattering vector ($q = 4\pi\sin\theta/\lambda$, where θ is half of the scattering angle and λ is x-ray wavelength.) using the software equipped at the beamline. In-situ stretching-SAXS measurements were based on a stretch station which can be controlled by wireless. SAXS data were recorded at different strain. For relaxation mode, the specimen was stretched to a strain of $\lambda = 4.5$, and then SAXS data were recorded during different relaxation time. The 2D SAXS scattering data were transformed into 1D SAXS curves by the default software of the SAXS apparatus.

Photo-induced mechanical force testing. As for photo-induced mechanical force, we carried out measurements at room temperature to monitor the light-generated force of TA- WS₂/PU film by applying NIR light (808 nm) to a strip-shaped sample (15 mm × 2 mm × 0.05 mm) held above an analytical balance, the photo-induced mechanical force generated in the sample sheet can be sensed and measured from the following formula:

$$F = mg$$

Where m is a real-time indicator of the balance, g is the acceleration of gravity.

Data availability. The data that support the findings of this study are available from the corresponding author upon request.

References

1. Chen, S. *et al.* Mechanically and biologically skin-like elastomers for bio-integrated electronics. *Nat. Commun.* **11**, 1–8 (2020).
2. Chen, H., Song, Y., Cheng, X. & Zhang, H. Self-powered electronic skin based on the triboelectric generator. *Nano Energy* **56**, 252–268 (2019).
3. Li, Z. *et al.* All - Fiber Structured Electronic Skin with High Elasticity and Breathability. *Adv. Funct. Mater.* **30**, 1908411 (2020).
4. Kang, J. *et al.* Tough and Water-Insensitive Self-Healing Elastomer for Robust Electronic Skin. *Adv. Mater.* **30**, 1706846 (2018).
5. Lei, Z. & Wu, P. A supramolecular biomimetic skin combining a wide spectrum of mechanical properties and multiple sensory capabilities. *Nat. Commun.* **9**, 1–7 (2018).
6. Guo, Q. *et al.* A cephalopod-inspired mechanoluminescence material with skin-like self-healing and sensing properties. *Mater. Horizons* **6**, 996–1004 (2019).
7. Lei, Z. & Wu, P. A highly transparent and ultra-stretchable conductor with stable conductivity during large deformation. *Nat. Commun.* **10**, 1–9 (2019).
8. Zhang, L. *et al.* A Highly Efficient Self-Healing Elastomer with Unprecedented Mechanical Properties. *Adv. Mater.* **31**, 1901402 (2019).
9. Liu, Z. *et al.* Towards wearable electronic devices: A quasi-solid-state aqueous lithium-ion battery with outstanding stability, flexibility, safety and breathability. *Nano Energy* **44**, 164–173 (2018).
10. Salauddin, M. *et al.* Miniaturized springless hybrid nanogenerator for powering portable and wearable electronic devices from human-body-induced vibration. *Nano Energy* **51**, 61–72 (2018).
11. Tian, B., Liu, Q., Luo, C., Feng, Y. & Wu, W. Multifunctional Ultrastretchable Printed Soft Electronic Devices for Wearable Applications. *Adv. Electron. Mater.* **6**, 1900922 (2020).
12. Lee, J., Llerena Zambrano, B., Woo, J., Yoon, K. & Lee, T. Recent Advances in 1D Stretchable Electrodes and Devices for Textile and Wearable Electronics: Materials, Fabrications, and Applications. *Advanced Materials* **32**, 1902532 (2020).
13. Han, B. *et al.* Plasmonic - Assisted Graphene Oxide Artificial Muscles. *Adv. Mater.* **31**, 1806386 (2018).
14. Lee, J. A. *et al.* Electrochemically Powered, Energy-Conserving Carbon Nanotube

- Artificial Muscles. *Adv. Mater.* **29**, 1700870 (2017).
15. Yu, Q. *et al.* Fabrication of Light-Triggered Soft Artificial Muscles via a Mixed-Matrix Membrane Strategy. *Angew. Chemie Int. Ed.* **57**, 10192–10196 (2018).
16. Duduta, M., Hajiesmaili, E., Zhao, H., Wood, R. J. & Clarke, D. R. Realizing the potential of dielectric elastomer artificial muscles. *Proc. Natl. Acad. Sci. U. S. A.* **116**, 2476–2481 (2019).
17. Maziz, A. *et al.* Knitting and weaving artificial muscles. *Sci. Adv.* **3**, e1600327 (2017).
18. Umrao, S. *et al.* MXene artificial muscles based on ionically cross-linked Ti₃C₂Tx electrode for kinetic soft robotics. *Sci. Robot.* **4**, (2019).
19. Cao, J. *et al.* Arbitrarily 3D Configurable Hygroscopic Robots with a Covalent–Noncovalent Interpenetrating Network and Self-Healing Ability. *Adv. Mater.* **31**, 1–8 (2019).
20. Cao, J. *et al.* Ultrarobust Ti₃C₂TxMXene-Based Soft Actuators via Bamboo-Inspired Mesoscale Assembly of Hybrid Nanostructures. *ACS Nano* **14**, 7055–7065 (2020).
21. Lei, Z., Wang, Q., Sun, S., Zhu, W. & Wu, P. A Bioinspired Mineral Hydrogel as a Self-Healable, Mechanically Adaptable Ionic Skin for Highly Sensitive Pressure Sensing. *Adv. Mater.* **29**, 1700321 (2017).
22. Rao, Y. L. *et al.* Stretchable self-healing polymeric dielectrics cross-linked through metal-ligand coordination. *J. Am. Chem. Soc.* **138**, 6020–6027 (2016).
23. Zhao, Y. *et al.* A Self-Healing Aqueous Lithium-Ion Battery. *Angew. Chemie - Int. Ed.* **55**, 14384–14388 (2016).
24. Cao, Y. *et al.* A Highly Stretchy, Transparent Elastomer with the Capability to Automatically Self-Heal Underwater. *Adv. Mater.* **30**, 1804602 (2018).
25. Liao, M. *et al.* Wearable, Healable, and Adhesive Epidermal Sensors Assembled from Mussel-Inspired Conductive Hybrid Hydrogel Framework. *Adv. Funct. Mater.* **27**, 1703852 (2017).
26. Cao, J. *et al.* Multiple Hydrogen Bonding Enables the Self-Healing of Sensors for Human–Machine Interactions. *Angew. Chemie - Int. Ed.* **56**, 8795–8800 (2017).
27. Liu, X. *et al.* Hierarchically Structured Self-Healing Sensors with Tunable Positive/Negative Piezoresistivity. *Adv. Funct. Mater.* **28**, 1–10 (2018).
28. Son, D. *et al.* An integrated self-healable electronic skin system fabricated via dynamic reconstruction of a nanostructured conducting network. *Nat. Nanotechnol.* **13**, 1057–1065 (2018).
29. Wang, Z. *et al.* 3D-printable self-healing and mechanically reinforced hydrogels with host-guest non-covalent interactions integrated into covalently linked networks. *Mater. Horizons* **6**, 733–742 (2019).
30. Li, Y. *et al.* Self-Healing Hydrogel with a Double Dynamic Network Comprising Imine and Borate Ester Linkages. *Chem. Mater.* **31**, 5576–5583 (2019).
31. Wu, J., Cai, L. H. & Weitz, D. A. Tough Self-Healing Elastomers by Molecular Enforced Integration of Covalent and Reversible Networks. *Adv. Mater.* **29**, 1702616 (2017).
32. Li, C. *et al.* Supramolecular–covalent hybrid polymers for light-activated mechanical actuation. *Nat. Mater.* **19**, 900–909 (2020).
33. Yanagisawa, Y., Nan, Y., Okuro, K. & Aida, T. Mechanically robust, readily repairable polymers via tailored noncovalent cross-linking. *Science (80-.).* **359**, 72–76 (2018).

34. Qin, B. *et al.* Tough and Multi - Recyclable Cross - Linked Supramolecular Polyureas via Incorporating Noncovalent Bonds into Main - Chains. *Adv. Mater.* **32**, 2000096 (2020).
35. King, D. R., Okumura, T., Takahashi, R., Kurokawa, T. & Gong, J. P. Macroscale Double Networks: Design Criteria for Optimizing Strength and Toughness. *ACS Appl. Mater. Interfaces* **11**, 35343–35353 (2019).
36. Li, X. *et al.* Mesoscale bicontinuous networks in self-healing hydrogels delay fatigue fracture. *Proc. Natl. Acad. Sci. U. S. A.* **117**, 7606–7612 (2020).
37. Hubbard, A. M. *et al.* Hydrogel/Elastomer Laminates Bonded via Fabric Interphases for Stimuli-Responsive Actuators. *Matter* **1**, 674–689 (2019).
38. Cui, W. *et al.* Fiber-Reinforced Viscoelastomers Show Extraordinary Crack Resistance That Exceeds Metals. *Adv. Mater.* **32**, 1907180 (2020).
39. Zhang, C. *et al.* Polyphenol-Assisted Exfoliation of Transition Metal Dichalcogenides into Nanosheets as Photothermal Nanocarriers for Enhanced Antibiofilm Activity. *ACS Nano* **12**, 12347–12356 (2018).
40. Ramakrishna Matte, H. S. S. *et al.* MoS₂ and WS₂ analogues of graphene. *Angew. Chemie - Int. Ed.* **49**, 4059–4062 (2010).
41. Pan, L., Liu, Y. T., Xie, X. M. & Ye, X. Y. Facile and Green Production of Impurity-Free Aqueous Solutions of WS₂ Nanosheets by Direct Exfoliation in Water. *Small* **12**, 6703–6713 (2016).
42. Lee, C. *et al.* Anomalous lattice vibrations of single- and few-layer MoS₂. *ACS Nano* **4**, 2695–2700 (2010).
43. Late, D. J., Liu, B., Matte, H. S. S. R., Rao, C. N. R. & Dravid, V. P. Rapid characterization of ultrathin layers of chalcogenides on SiO₂/Si substrates. *Adv. Funct. Mater.* **22**, 1894–1905 (2012).
44. Xu, D. *et al.* High Yield Exfoliation of WS₂ Crystals into 1-2 Layer Semiconducting Nanosheets and Efficient Photocatalytic Hydrogen Evolution from WS₂/CdS Nanorod Composites. *ACS Appl. Mater. Interfaces* **10**, 2810–2818 (2018).
45. Elías, A. L. *et al.* Controlled synthesis and transfer of large-area WS₂ sheets: From single layer to few layers. *ACS Nano* **7**, 5235–5242 (2013).
46. Niu, W. *et al.* Remalleable, Healable, and Highly Sustainable Supramolecular Polymeric Materials Combining Superhigh Strength and Ultrahigh Toughness. *ACS Appl. Mater. Interfaces* **12**, 30805–30814 (2020).
47. Wei, Q. & Haag, R. Universal polymer coatings and their representative biomedical applications. *Materials Horizons* **2**, 567–577 (2015).
48. Su, G., Zhou, T., Liu, X. & Zhang, Y. Two-step volume phase transition mechanism of poly(N-vinylcaprolactam) hydrogel online-tracked by two-dimensional correlation spectroscopy. *Phys. Chem. Chem. Phys.* **19**, 27221–27232 (2017).
49. Ying, W. Bin *et al.* Waterproof, Highly Tough, and Fast Self-Healing Polyurethane for Durable Electronic Skin. *ACS Appl. Mater. Interfaces* **12**, 11072–11083 (2020).
50. Guo, Y. *et al.* Asynchronous fracture of hierarchical microstructures in hard domain of thermoplastic polyurethane elastomer: Effect of chain extender. *Polymer (Guildf)*. **138**, 242–254 (2018).
51. Xu, W. *et al.* A Multiscale Investigation on the Mechanism of Shape Recovery for IPDI to PPDI Hard Segment Substitution in Polyurethane. *Macromolecules* **49**, 5931–

- 5944 (2016).
52. Ma, X., Qu, X., Zhang, Q. & Chen, F. Analysis of interfacial action of rectorite/thermoplastic polyurethane nanocomposites by inverse gas chromatography and molecular simulation. *Polymer (Guildf)*. **49**, 3590–3600 (2008).
53. Toth, R. *et al.* Computer simulation of polypropylene/organoclay nanocomposites: Characterization of atomic scale structure and prediction of binding energy. *Polymer (Guildf)*. **45**, 8075–8083 (2004).
54. Ansari, S., Kelarakis, A., Estevez, L. & Giannelis, E. P. Oriented arrays of graphene in a polymer matrix by in situ reduction of graphite oxide nanosheets. *Small* **6**, 205–209 (2010).
55. Blundell, D. J., Eeckhaut, G., Fuller, W., Mahendrasingam, A. & Martin, C. Real time SAXS/stress-strain studies of thermoplastic polyurethanes at large strains. *Polymer (Guildf)*. **43**, 5197–5207 (2002).
56. Wang, Y. *et al.* Hierarchically Structured Self-Healing Actuators with Superfast Light- and Magnetic-Response. *Adv. Funct. Mater.* **29**, 1906198 (2019).
57. Xu, W. M., Rong, M. Z. & Zhang, M. Q. Sunlight driven self-healing, reshaping and recycling of a robust, transparent and yellowing-resistant polymer. *J. Mater. Chem. A* **4**, 10683–10690 (2016).
58. Si, Q. *et al.* Controllable and Stable Deformation of a Self-Healing Photo-Responsive Supramolecular Assembly for an Optically Actuated Manipulator Arm. *ACS Appl. Mater. Interfaces* **10**, 29909–29917 (2018).
59. Wang, H. *et al.* Synthesis of Self-Healing Polymers by Scandium-Catalyzed Copolymerization of Ethylene and Anisylpropylenes. *J. Am. Chem. Soc.* **141**, 3249–3257 (2019).
60. Kim, S. M. *et al.* Superior Toughness and Fast Self-Healing at Room Temperature Engineered by Transparent Elastomers. *Adv. Mater.* **30**, 1705145 (2018).
61. Kang, J. *et al.* Tough and Water-Insensitive Self-Healing Elastomer for Robust Electronic Skin. *Adv. Mater.* **30**, 1706846 (2018).
62. Song, P., Qin, H., Gao, H. L., Cong, H. P. & Yu, S. H. Self-healing and superstretchable conductors from hierarchical nanowire assemblies. *Nat. Commun.* **9**, 1–9 (2018).

Acknowledgements

The authors thank the National Natural Science Foundation of China (51873123, 51673121), and the State Key Laboratory of Polymer Materials Engineering (Grant sklpme2019-2-20) for financial support. The authors also thank Dr. Guiping Yuan from the Analytical and Testing Centre of Sichuan University for providing the TEM measurement.

Author contributions

X.Z. supervised the project. X.Z. and Y.W. conceived the project. Y.W. performed the experiments and wrote the paper. X.H. performed binding energy simulation. Data analysis was performed by Y.W. Y.W. wrote the paper and others revised the manuscript and provided some suggestions.

Additional information

Supplementary Information accompanies this paper at <http://www.nature.com/naturecommunications>

Competing financial interests: The authors declare no competing financial interests.

Reprints and permission information is available online at <http://npg.nature.com/reprintsandpermissions/>

How to cite this article:

Publisher's note: Springer Nature remains neutral with regard to jurisdictional claims in published maps and institutional affiliations.

Figures

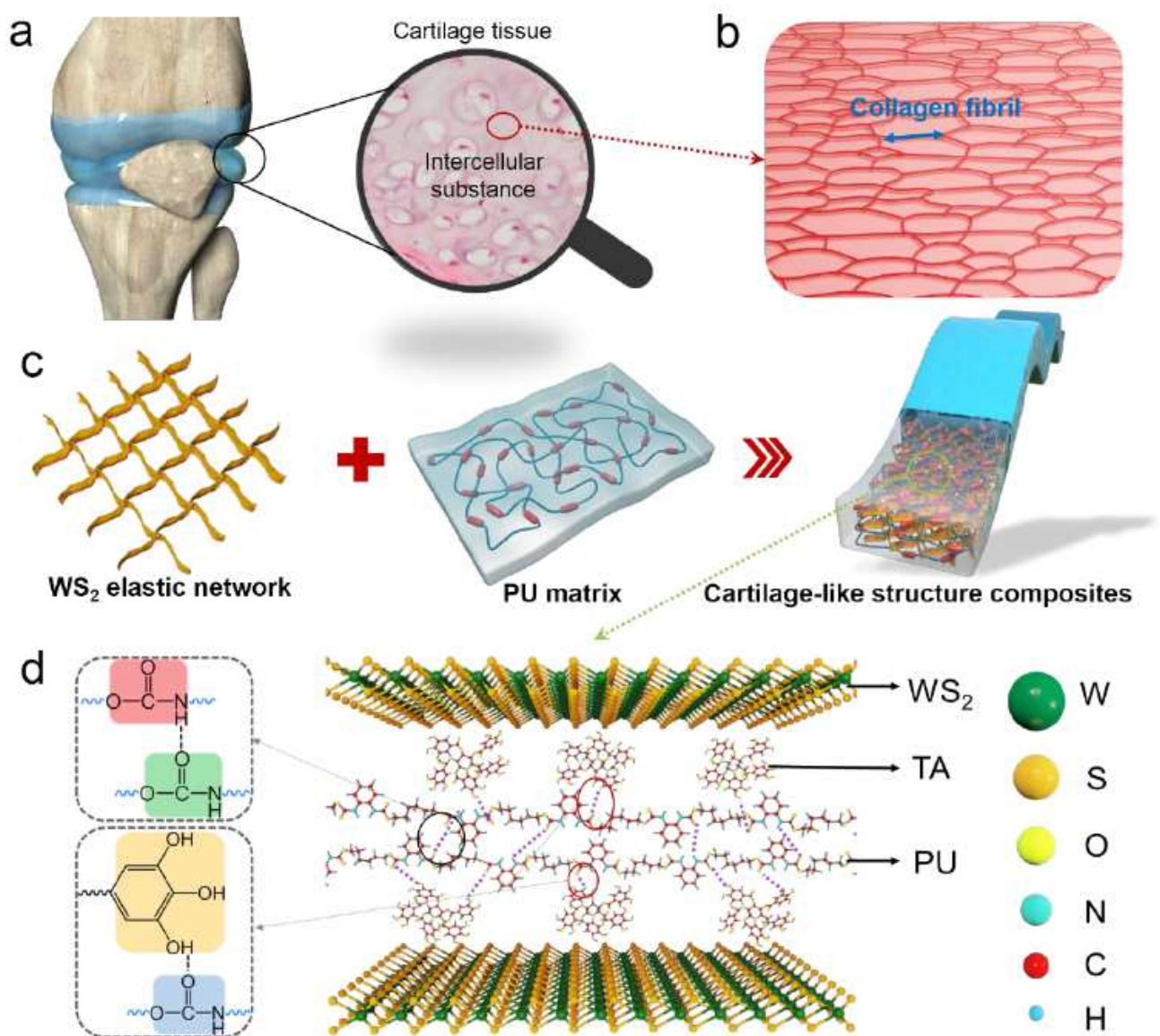


Figure 1

The nanostructure design of the cartilage-like PU composite. **a** Schematic illustration of a cartilage structure. **b** Schematic illustration of intercellular substance of cartilage tissue. **c** Schematic illustration of the nanostructure of composite consisting of hydrogen bonded interwoven network of 2D WS_2 and PU matrix. **d** Schematics of the dynamic noncovalent bonding interaction between PU and interwoven network of 2D WS_2 .

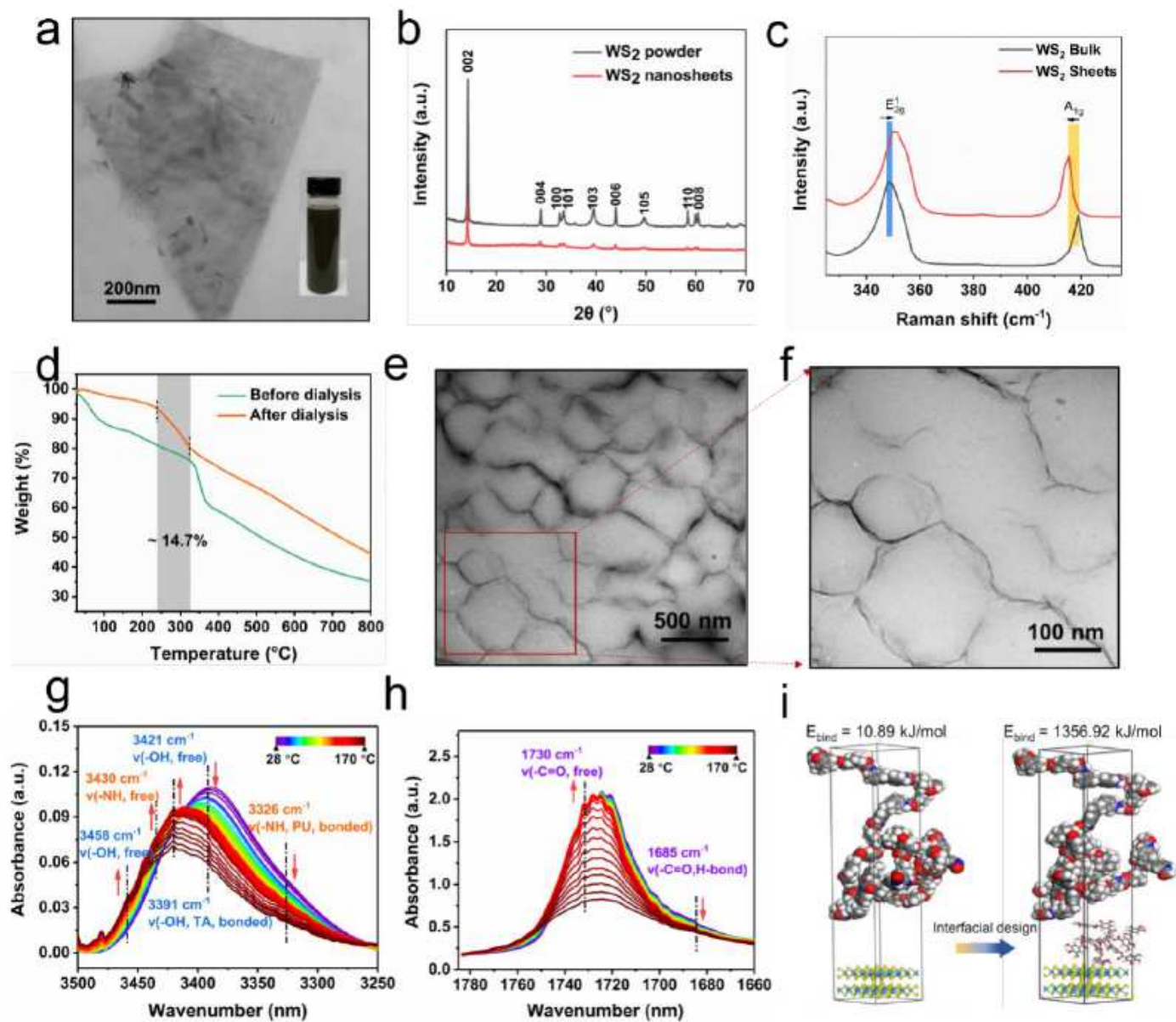


Figure 2

Structural and compositional characterizations. a High-resolution TEM images of the exfoliated WS₂ nanosheet. b XRD patterns of WS₂ powder and WS₂ nanosheets. c Raman spectra of WS₂ bulk and nanosheets. d TGA curve of TA-WS₂ nanosheets before and after dialysis. e, f TEM images of TA-WS₂/PU composites with 3D conductive network. g, h Temperature-dependent FTIR spectra of WS₂/PU nanocomposites upon heating from 25 to 170 °C, (g) 3250-3500 cm⁻¹ and (h) 1660-1780 cm⁻¹. i Optimized structures and binding energies of the before and after interfacial design.

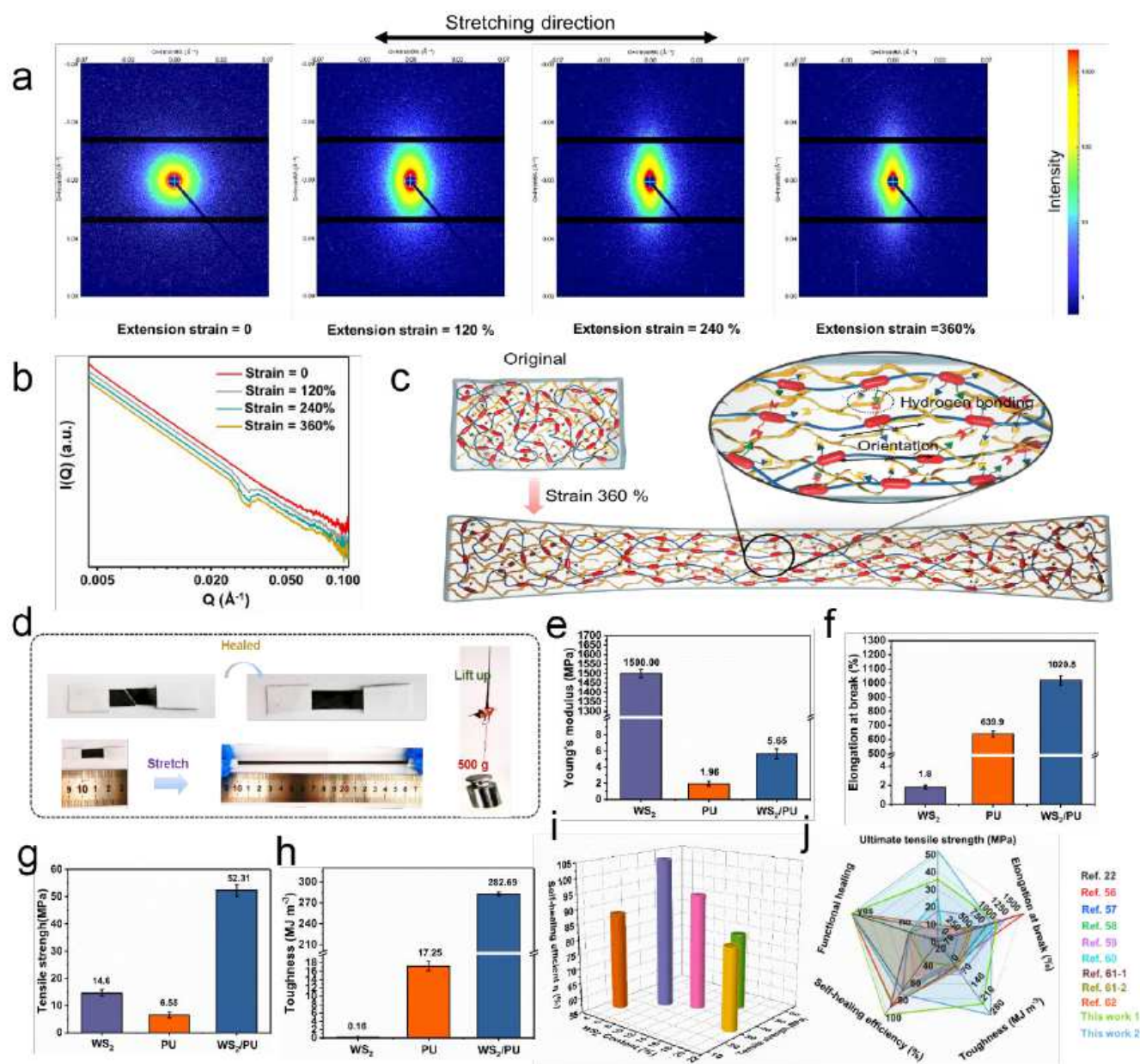


Figure 3

Mechanical and self-healing performances. a 2D SAXS images of the TA-WS₂/PU with different extension strain during uniaxial stretching process. b 1D scattering profiles of TA-WS₂/PU integrated from 2D SAXS patterns under different strains. c Schematic illustrations of the nanostructure of the original sample and stretching sample. d Photographs demonstrating excellent mechanical property of self-healed TA-WS₂/PU composites when stretched and lift a weight. e-h Comparison of (e) Young's modulus, (f) elongation at break, (g) ultimate tensile strength, and (h) toughness of the pure WS₂, PU, and TA-WS₂/PU nanocomposite. i Comparison of tensile strength and self-healing efficiency of our TA-WS₂/PU nanocomposite with different filler content. j Comparison of Young's modulus, elongation at break, ultimate tensile strength, toughness, self-healing efficiency, and functional healing ability of our nanocomposite with other self-healing materials.

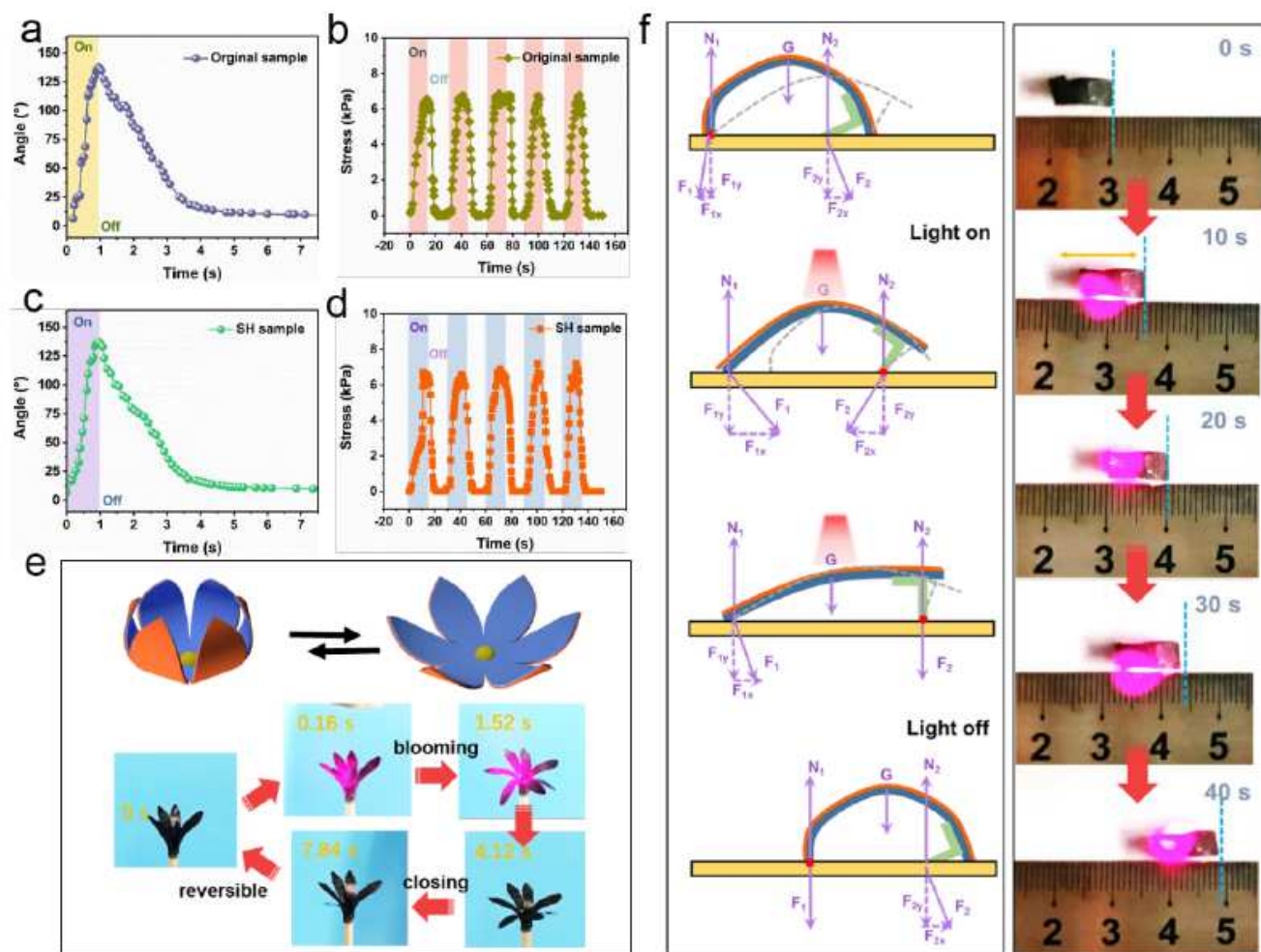


Figure 4

NIR light actuating and self-healing performances. a, c Time dependence of the bending angle of (a) the original sample and (c) SH sample exposed to NIR light when the light is switched on and off. b, d Actuation stress as a function of time as NIR light is periodically turned on (time, 15 s) and off (time, 15 s) on (b) the original and (d) SH sample. e Photographs of a “flower” blooming and closing stimulated by NIR light. f A crawling robot is able to continually crawl forward under periodic NIR light on and off.

Supplementary Files

This is a list of supplementary files associated with this preprint. Click to download.

- [SupplementaryInformation.docx](#)
- [Movie1.mp4](#)
- [Movie2.mp4](#)